

Supplementary Materials: Comparing proton momentum distributions in $A = 3$ nuclei via ${}^3\text{He}$ and ${}^3\text{H}(e, e'p)$ measurements

CROSS-SECTION RATIO EXTRACTION

We extracted the ${}^3\text{He}(e, e'p) / {}^3\text{H}(e, e'p)$ cross-section ratio, as a function of missing momentum $\sigma_{{}^3\text{He}(e, e'p)} / \sigma_{{}^3\text{H}(e, e'p)}(p_{\text{miss}})$, from the measured normalized event yield ratio $R_{{}^3\text{He}/{}^3\text{H}}^{\text{corr.yield}}(p_{\text{miss}})$ by applying corrections for radiative effects, bin-migration, and finite E_{miss} acceptance. These corrections were applied in a multiplicative manner:

$$R_{n(p)}^{\text{meas.}}(p_{\text{miss}}) = R_{{}^3\text{He}/{}^3\text{H}}^{\text{corr.yield}}(p_{\text{miss}}) \times C_{\text{BinMig}} \times C_{\text{Rad}} \times C_{E_m\text{Acc}}, \quad (1)$$

with:

$$C_{\text{BinMig}} = R_{\text{Sim}}^{\sigma_{\text{Rad}}}(p_{\text{miss}}^{\text{gen}}) / R_{\text{Sim}}^{\sigma_{\text{Rad}}}(p_{\text{miss}}^{\text{rec}}), \quad (2)$$

$$C_{\text{Rad}} = R_{\text{Sim}}^{\sigma_{\text{Born}}}(p_{\text{miss}}^{\text{gen}}) / R_{\text{Sim}}^{\sigma_{\text{Rad}}}(p_{\text{miss}}^{\text{gen}}), \quad (3)$$

$$C_{E_m\text{Acc}} = n_{{}^3\text{He}/{}^3\text{H}}(p_{\text{miss}}^{\text{gen}}) / R_{\text{Sim}}^{\sigma_{\text{Born}}}(p_{\text{miss}}^{\text{gen}}), \quad (4)$$

where $R_{\text{Sim}}(p_{\text{miss}})$ is the SIMC calculated ${}^3\text{He} / {}^3\text{H}$ event yield ratio, σ_{Rad} and σ_{Born} mark calculations with and without radiation effects, and $p_{\text{miss}}^{\text{rec}}$ and $p_{\text{miss}}^{\text{gen}}$ imply using the generated and reconstructed p_{miss} values of each event in the calculation. $n_{{}^3\text{He}/{}^3\text{H}}(k)$ is the ratio of the ${}^3\text{He} / {}^3\text{H}$ proton momentum distributions obtained from integrating the spectral function used by SIMC. As can be seen, most terms in the different correction factors cancel to produce a final correction of: $n_{{}^3\text{He}/{}^3\text{H}}(p_{\text{miss}}^{\text{gen}}) / R_{\text{Sim}}^{\sigma_{\text{Rad}}}(p_{\text{miss}}^{\text{rec}})$.

Figure 1 shows the individual correction terms and the final correction term as a function of p_{miss} . As can be seen, the individual correction terms, as well as the total correction, are bounded by $\pm 10\%$. We assume a point-to-point systematic uncertainty on the final correction in each p_{miss} bin to equal 20% of the size of the correction. Table I lists the values of the correction terms and the resulting cross-section ratio and uncertainties for each p_{miss} bin.

The other source of point-to-point systematic uncertainty on the extracted cross-section ratio is due to the event selection criteria (momentum and angular acceptances, and θ_{r_q} and x_B limits). This uncertainty was extracted by repeating the analysis 5000 times, each time randomly selecting a different value for each criterion within an interval of: $4.0 \pm 0.5\%$ for the momentum acceptance; 27.5 ± 2.5 mrad and 55.0 ± 5 mrad for the in- and out-of-plane angular acceptance respectively; $37.5 \pm 2.5^\circ$ for the θ_{r_q} upper limit; and 1.3 ± 0.025 for the x_B lower limit. For each missing momentum bin, we histogrammed all resulting ratios and took the standard deviation of the ratio distribution as the systematic uncertainty from varying the acceptance and kinematical cuts.

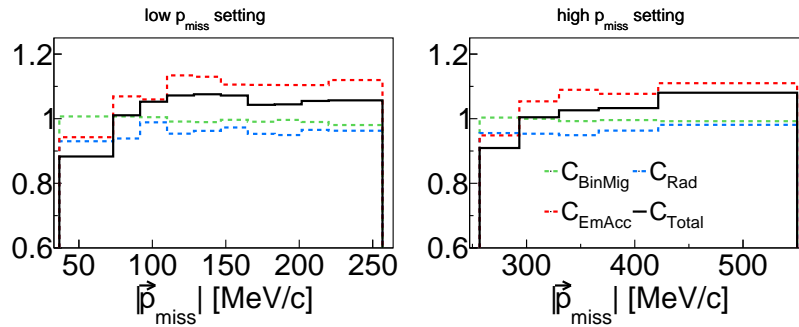


FIG. 1: Corrections applied to the normalized event yield ratio $R_{{}^3\text{He}/{}^3\text{H}}^{\text{corr.yield}}(p_{\text{miss}})$.

CALCULATED MOMENTUM DISTRIBUTION RATIOS

The extracted cross-section ratios are compared with several momentum distribution ratios obtained from Quantum Monte Carlo calculations using the AV18+UX and N^2LO interactions. The latter includes both two- and three-body

TABLE I: Values from Figures 2 and 3 in the main text. The first and second columns correspond to the p_{miss} range and mean values respectively. The third column corresponds to the ratio of measured ${}^3\text{He}$ ($e, e'p$) to ${}^3\text{H}$ ($e, e'p$) normalized event yields $R_{3\text{He}/3\text{H}}^{corr.yield}$ with the corresponding statistical and systematic uncertainties. The fourth column corresponds to the ratio of extracted ${}^3\text{He}$ to ${}^3\text{H}$ momentum distributions $\sigma_{3\text{He}(e,e'p)}/\sigma_{3\text{H}(e,e'p)}$ with the corresponding statistical and systematic uncertainties. The fifth column corresponds to the simulated ratio of ${}^3\text{He}$ ($e, e'p$) to ${}^3\text{H}$ ($e, e'p$) normalized event yields $R_{Sim}^{\sigma rad}$.

p_{miss} range (MeV/c)	p_{miss} mean (MeV/c)	$R_{3\text{He}/3\text{H}}^{corr.yield}$ (Fig. 2)	$\sigma_{3\text{He}(e,e'p)}/\sigma_{3\text{H}(e,e'p)}$ (Fig. 3)	$R_{Sim}^{\sigma rad}$ (Fig. 2)
36.67 - 73.33	63.01	$2.88 \pm 0.13 \pm 0.04$	$2.54 \pm 0.11 \pm 0.12$	2.79
73.33 - 91.67	83.04	$2.59 \pm 0.09 \pm 0.02$	$2.61 \pm 0.09 \pm 0.04$	2.17
91.67 - 110.00	100.72	$1.97 \pm 0.06 \pm 0.01$	$2.07 \pm 0.06 \pm 0.03$	1.92
110.00 - 128.33	118.82	$1.90 \pm 0.06 \pm 0.02$	$2.04 \pm 0.06 \pm 0.04$	1.76
128.33 - 146.67	136.99	$1.79 \pm 0.07 \pm 0.01$	$1.93 \pm 0.07 \pm 0.04$	1.66
146.67 - 165.00	155.17	$1.78 \pm 0.08 \pm 0.02$	$1.91 \pm 0.08 \pm 0.04$	1.59
165.00 - 183.33	173.51	$1.60 \pm 0.09 \pm 0.02$	$1.67 \pm 0.09 \pm 0.04$	1.57
183.33 - 201.67	191.74	$1.56 \pm 0.11 \pm 0.02$	$1.63 \pm 0.11 \pm 0.03$	1.51
201.67 - 220.00	209.95	$1.50 \pm 0.13 \pm 0.03$	$1.58 \pm 0.14 \pm 0.04$	1.44
220.00 - 256.67	234.83	$1.39 \pm 0.13 \pm 0.06$	$1.47 \pm 0.14 \pm 0.09$	1.36
256.67 - 293.33	277.52	$1.90 \pm 0.22 \pm 0.05$	$1.73 \pm 0.20 \pm 0.08$	1.43
293.33 - 330.00	311.11	$1.54 \pm 0.17 \pm 0.04$	$1.55 \pm 0.17 \pm 0.05$	1.18
330.00 - 366.67	346.78	$1.65 \pm 0.21 \pm 0.03$	$1.70 \pm 0.22 \pm 0.04$	1.07
366.67 - 421.67	392.49	$1.75 \pm 0.23 \pm 0.06$	$1.81 \pm 0.24 \pm 0.08$	1.03
421.67 - 550.00	454.74	$2.22 \pm 0.40 \pm 0.13$	$2.40 \pm 0.43 \pm 0.16$	1.04

terms and was calculated specifically for this work with a 1.0 fm cutoff and two parametrizations of the three-body contact term $E\tau$ and $E1$.

Fig. 2 shows the ratio of the calculated ${}^3\text{He}$ and ${}^3\text{H}$ proton and neutron momentum distributions obtained using the AV18+UX interaction and the two N^2LO interactions. While the individual momentum distributions vary by up to 20% between the two interactions, the quantity of interest for this work, i.e., the ${}^3\text{He} / {}^3\text{H}$ proton momentum distribution double ratio, varies less than 10% between the different interactions (red line in Fig. 2 right).

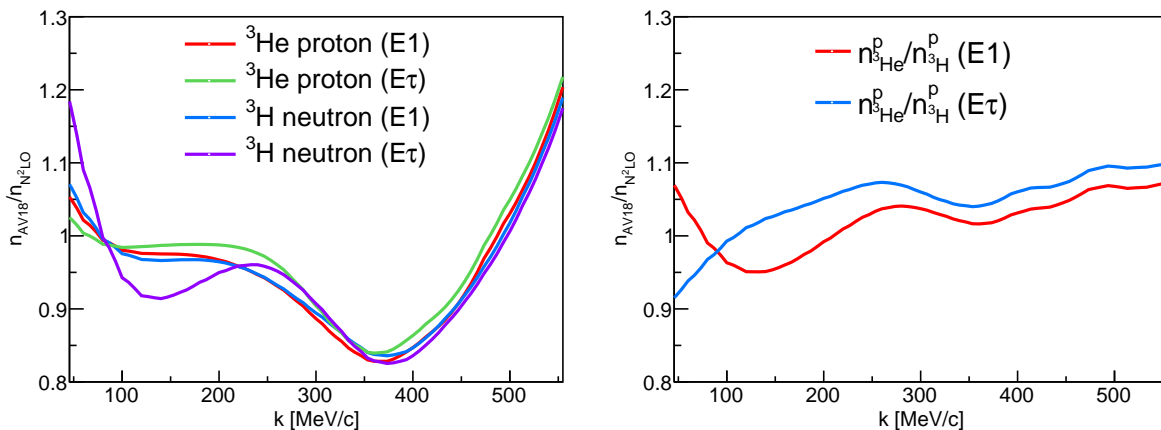


FIG. 2: Ratio of different distributions obtained using the AV18 and N^2LO potentials. The left figure shows the $(n_{A=3})_{AV18}/(n_{A=3})_{N^2LO}$, where $n_{A=3}$ refers to the ${}^3\text{He}$ proton and ${}^3\text{H}$ neutron momentum distributions. The right figure shows the double ratio $(n_{3\text{He}}^p/n_{3\text{H}}^p)_{AV18}/(n_{3\text{He}}^p/n_{3\text{H}}^p)_{N^2LO}$.

KINEMATICAL DISTRIBUTIONS

We compared the measured event yields for the ${}^3\text{H}$, and ${}^3\text{He}$ targets to the SIMC calculated yields to make sure that the simulation described the measured kinematical distributions well enough to be used to study the correction terms described above.

Figures 3-7 show the measured and calculated yields for various kinematical quantities. The simulated yields are scaled to match the measured integrated yield for each target and kinematics using scale factors of 0.60 and 0.59 (0.58

and 0.84) for the low p_{miss} and high p_{miss} ${}^3\text{H}$ (${}^3\text{He}$) kinematics respectively.

These scale factors imply that the measured and simulated ${}^3\text{He} / {}^3\text{H}$ yield ratios differ by 1% ($\approx 0.60/0.58$) and 30% ($\approx 0.59/0.84$). We examined these differences for a possible p_{miss} dependence and found that the data is consistent with a flat p_{miss} dependence (see Fig. 8). Specifically for the high- p_{miss} kinematics, fitting the double ratio to a constant and a linear function or p_{miss} gave reduced χ^2 of 0.97 and 0.94 respectively with the resulting slope of the linear function being consistent with zero within 1σ of its fit uncertainty.

Figures 9-16 show correlations between different measured kinematical quantities and their comparisons to simulation.

The simulation appears to agree with the distributions of the data well enough to use for computing the corrections described above.

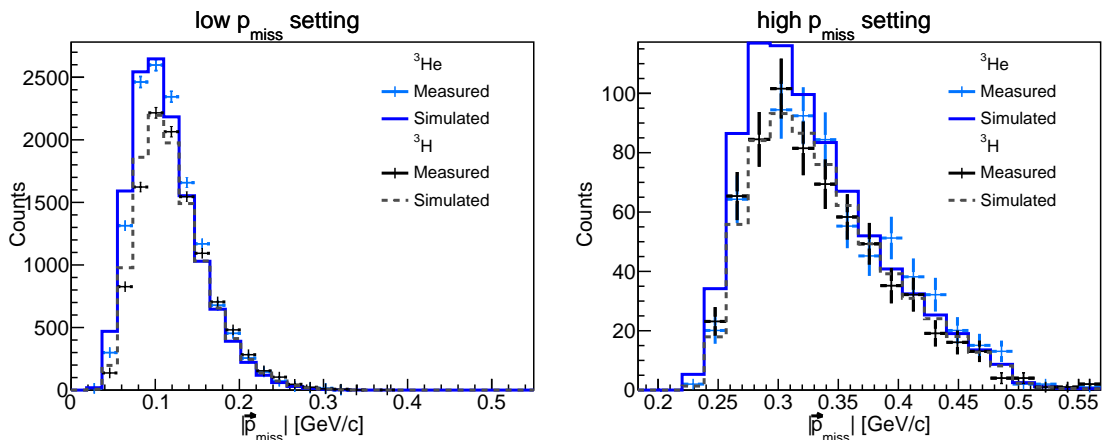


FIG. 3: Number of counts vs. p_{miss} for low p_{miss} (left) and high p_{miss} (right) settings. The blue markers and lines correspond to ${}^3\text{He}$ measured and simulated distributions respectively. The black markers and lines correspond to ${}^3\text{H}$ measured and simulated distributions respectively.

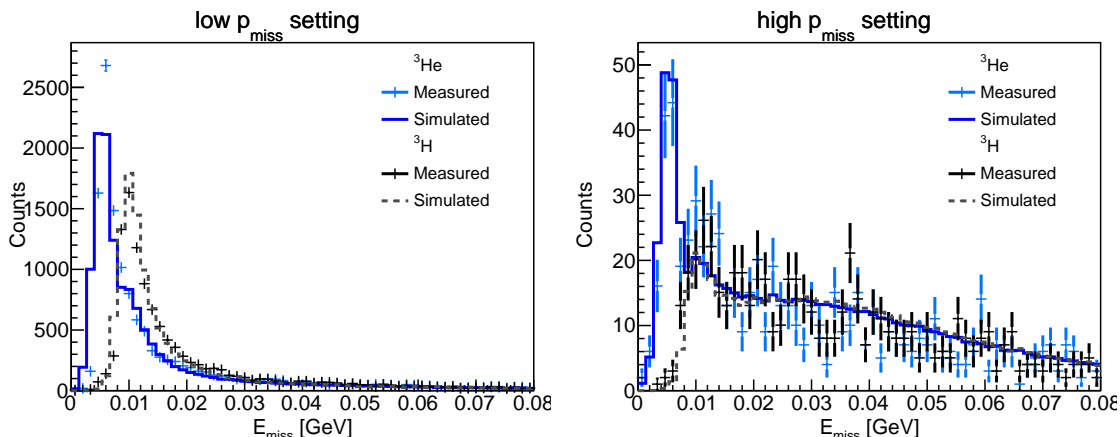


FIG. 4: Same as Fig. 3 only as a function of E_{miss} .

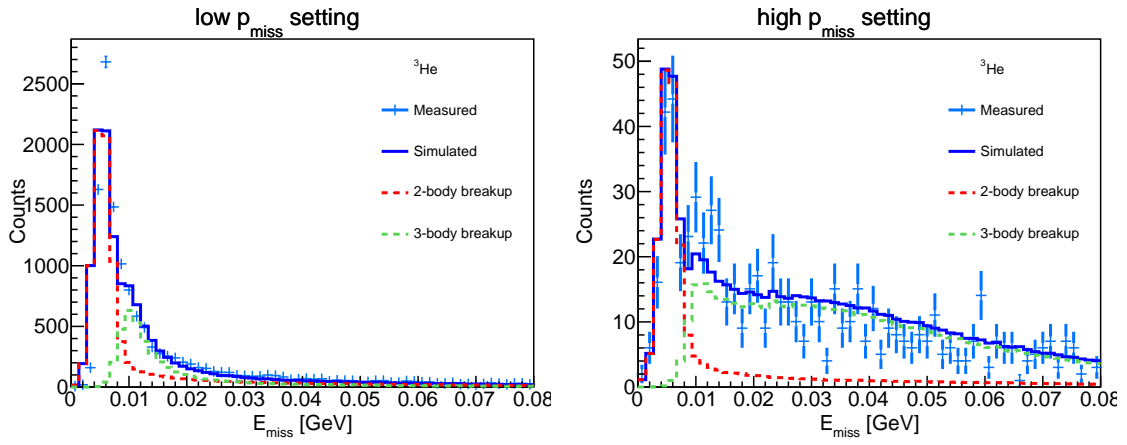


FIG. 5: Same as Fig. 3 only as a function of E_{miss} for ${}^3\text{He}$ only with separation of the SIMC yield to contributions from two- and three-body breakup.

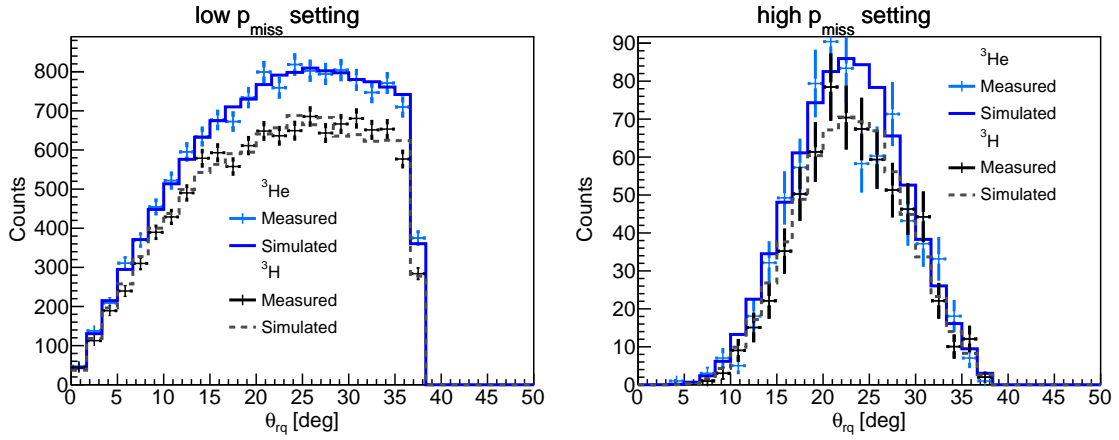


FIG. 6: Same as Fig. 3 only as a function of θ_{rq} .

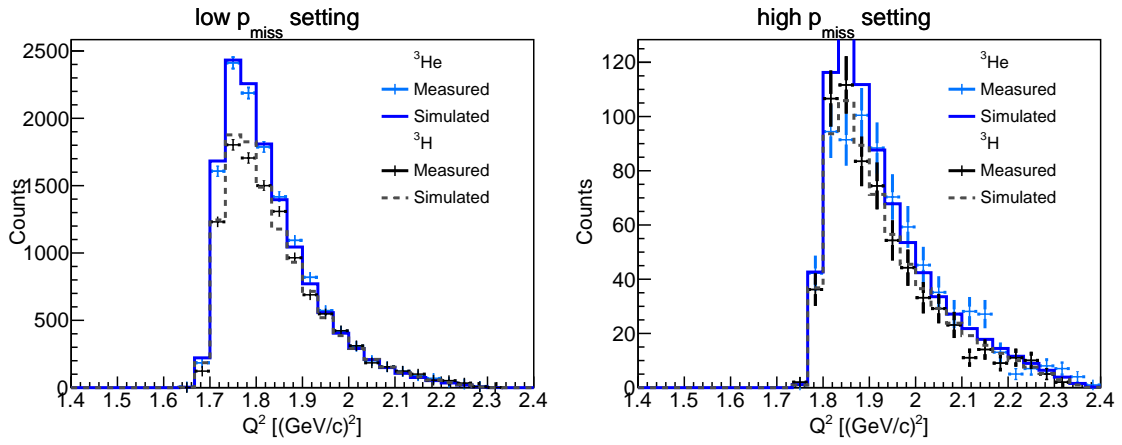


FIG. 7: Same as Fig. 3 only as a function of Q^2 .

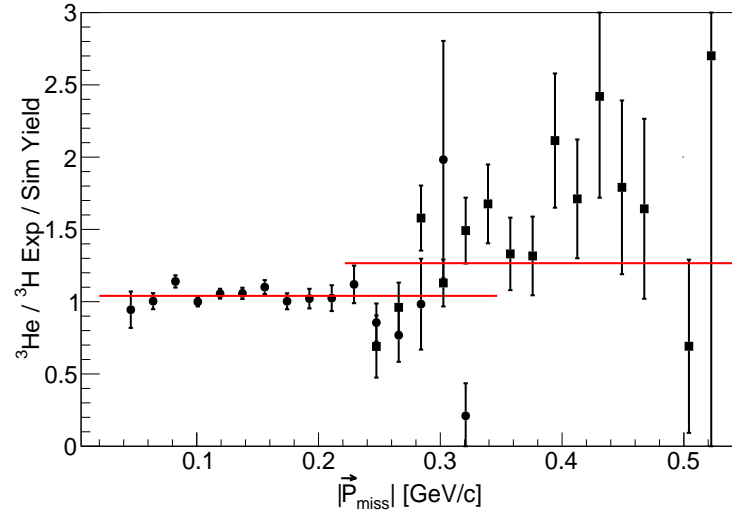


FIG. 8: p_{miss} dependence of the measured over simulated ${}^3\text{He} / {}^3\text{H}$ yield ratios from Fig 3. The red lines are the result of fits to a constant of each kinematics.

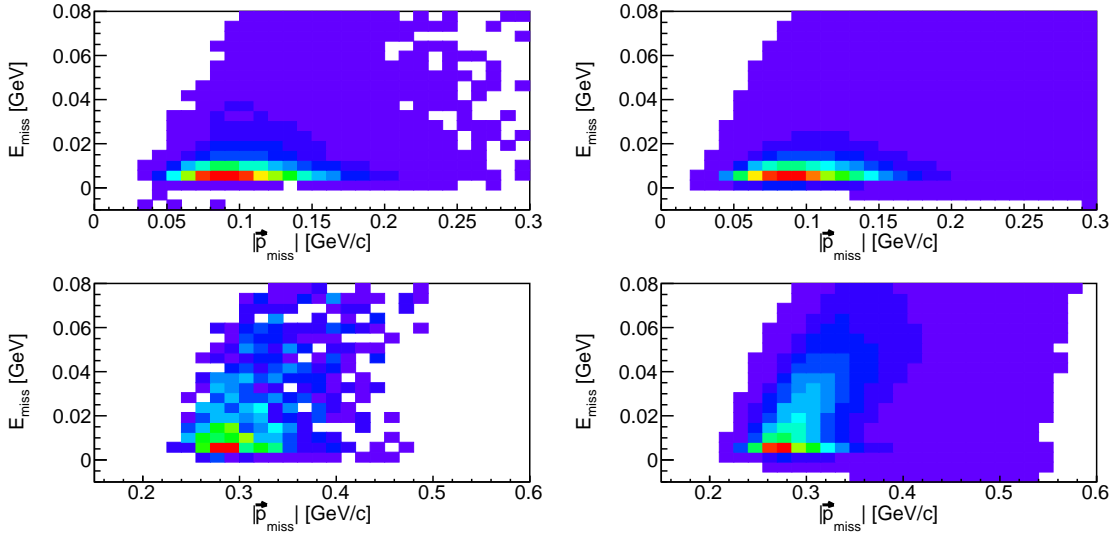


FIG. 9: ${}^3\text{He}$ E_{miss} vs. p_{miss} measured (left column) and simulated (right column). The top and bottom rows correspond to the low and high p_{miss} settings respectively.

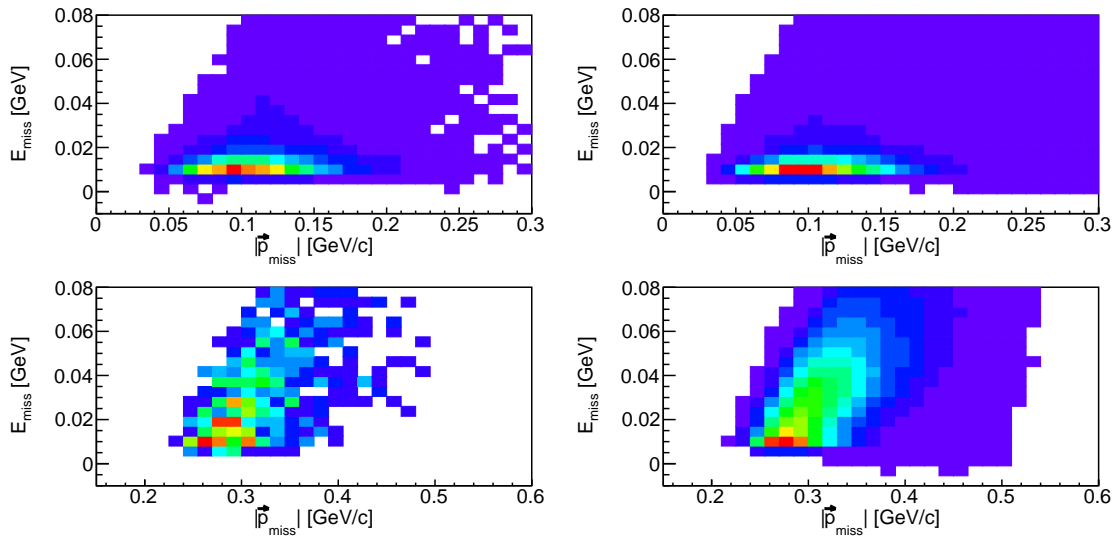


FIG. 10: Same as Fig. 9 only for ${}^3\text{H}$.

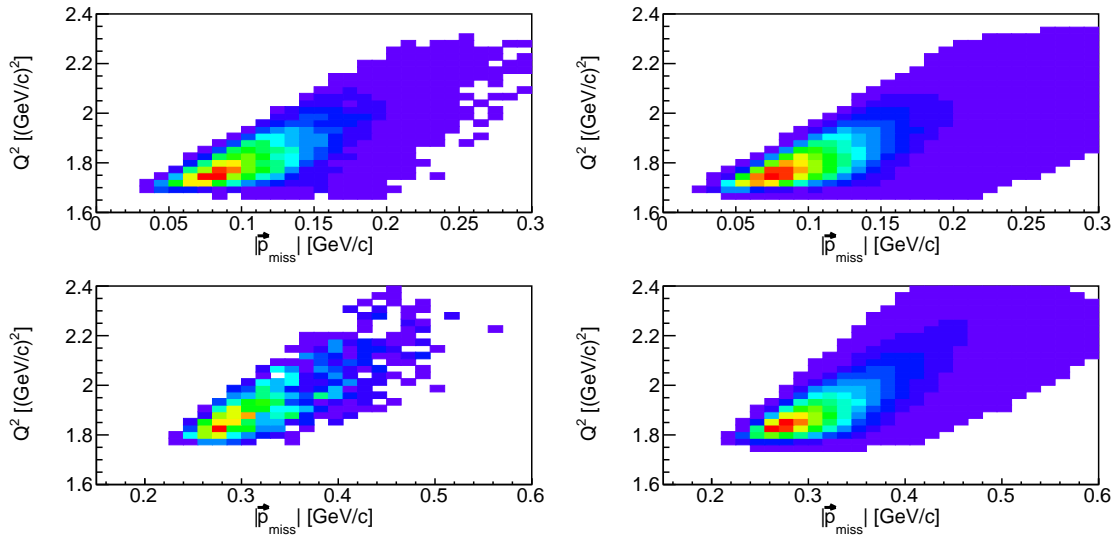


FIG. 11: ${}^3\text{He}$ Q^2 vs. p_{miss} measured (left column) and simulated (right column). The top and bottom rows correspond to the low and high p_{miss} settings respectively.

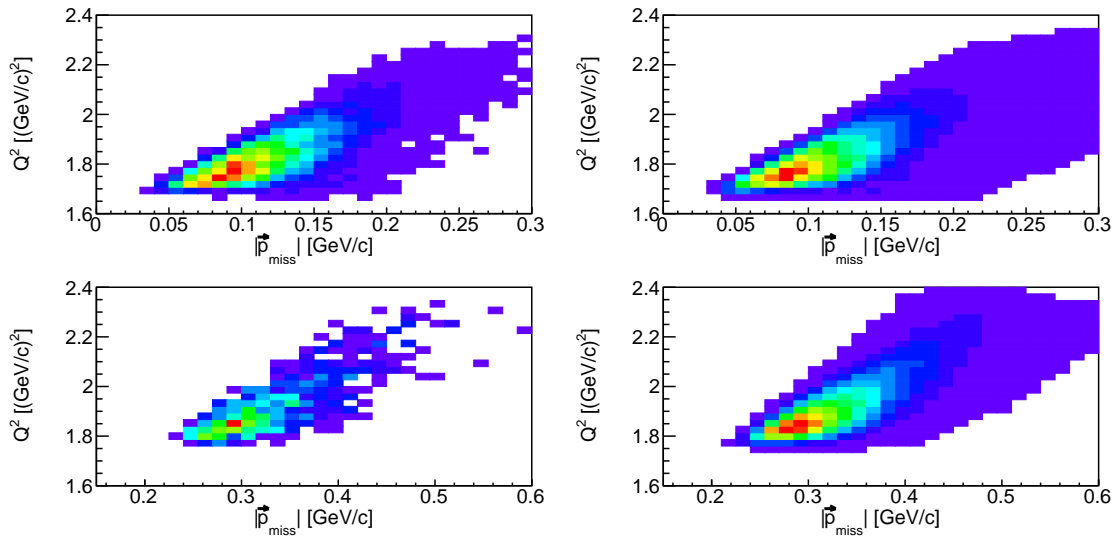


FIG. 12: Same as Fig. 11 only for ${}^3\text{H}$.

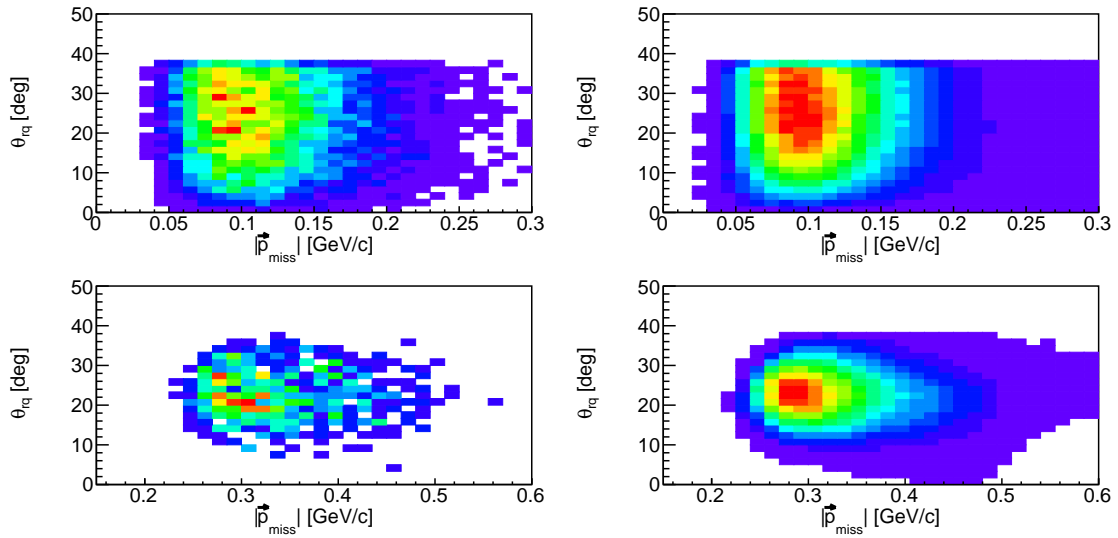


FIG. 13: ${}^3\text{He}$ θ_{rq} vs. p_{miss} measured (left column) and simulated (right column). The top and bottom rows correspond to the low and high p_{miss} settings respectively.

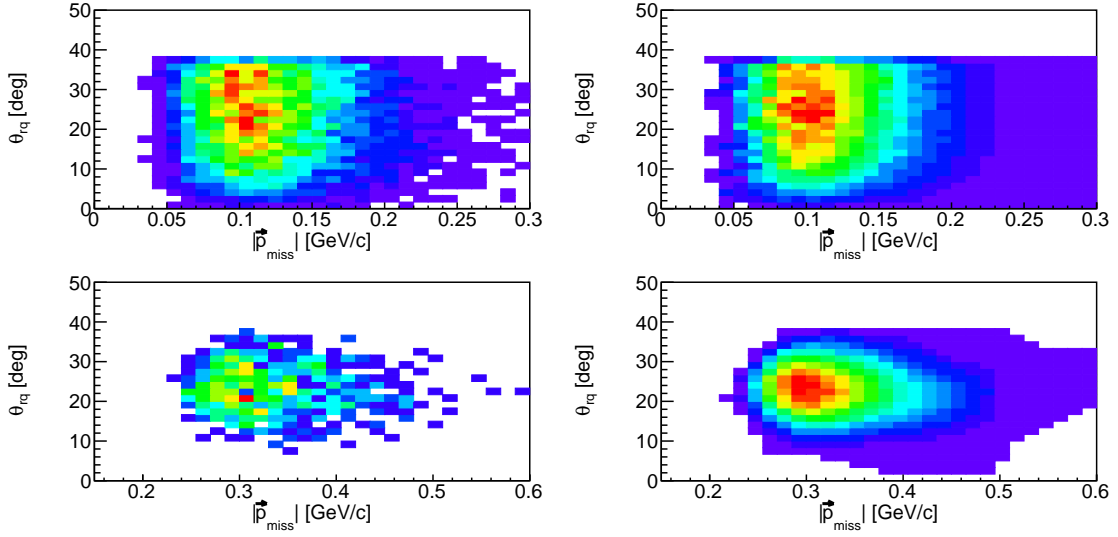


FIG. 14: Same as Fig. 13 only for ${}^3\text{H}$.

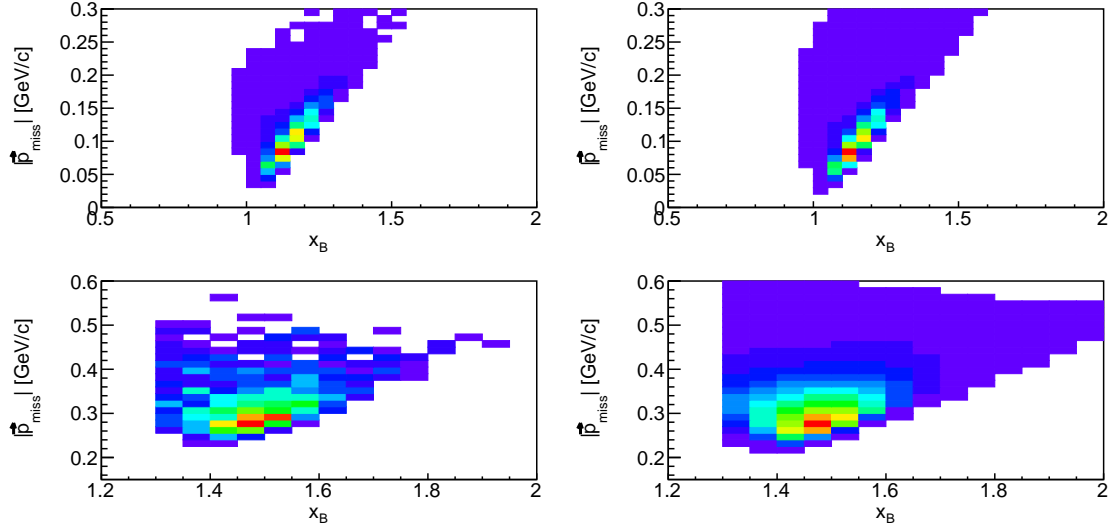


FIG. 15: ${}^3\text{He}$ p_{miss} vs. x_B measured (left column) and simulated (right column). The top and bottom rows correspond to the low and high p_{miss} settings respectively.

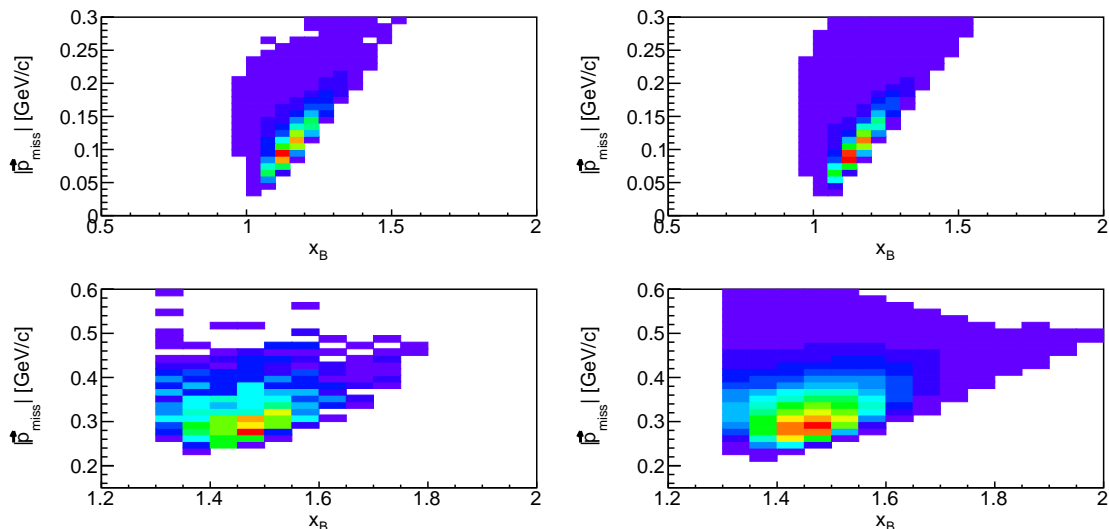


FIG. 16: Same as Fig. 16 only for ${}^3\text{H}$.

CALIBRATION AND RESOLUTIONS

Measurements of the exclusive $H(e, e')p$, $H(e, e')n$, and $d(e, e')n$ reactions were used to calibrate the two HRSs and determine their resolutions.

Fig. 17 and 18 show the measured $H(e, e')p$ missing mass and $H(e, e')p$ missing energy distributions. As can be seen, the $H(e, e')p$ missing mass is centered at the proton mass with a width smaller than 4 MeV. The $H(e, e')p$ missing energy distribution is offset from zero by less than 1 MeV with a width smaller than 1 MeV. The missing momentum distributions (individual components and total magnitude) for the $H(e, e')p$ reaction are shown in Fig 18 and are all centered at zero, as expected, with a narrow width of 2.3 – 6.7 MeV/c.

While kinematically over-constrained, the $H(e, e')p$ and $H(e, e')n$ reactions do not populate the entire acceptance of the HRSs. To this end, the $d(e, e')n$ reaction is used. As the missing-momentum distributions in this case do not have a simple expectation, the measured distributions are compared with a SIMC simulation using a deuteron momentum distribution calculated using the AV18 interaction. Fig. 19 shows the measured $d(e, e')n$ missing mass and energy. As can be seen, both are centered around the expected physical values with narrow width smaller than 1 MeV, in overall good agreement with the SIMC simulation (up to width $\ll 1$ MeV). Fig. 20 shows the measured $d(e, e')n$ missing momentum distributions that, as expected, also show good agreement with the SIMC simulation.

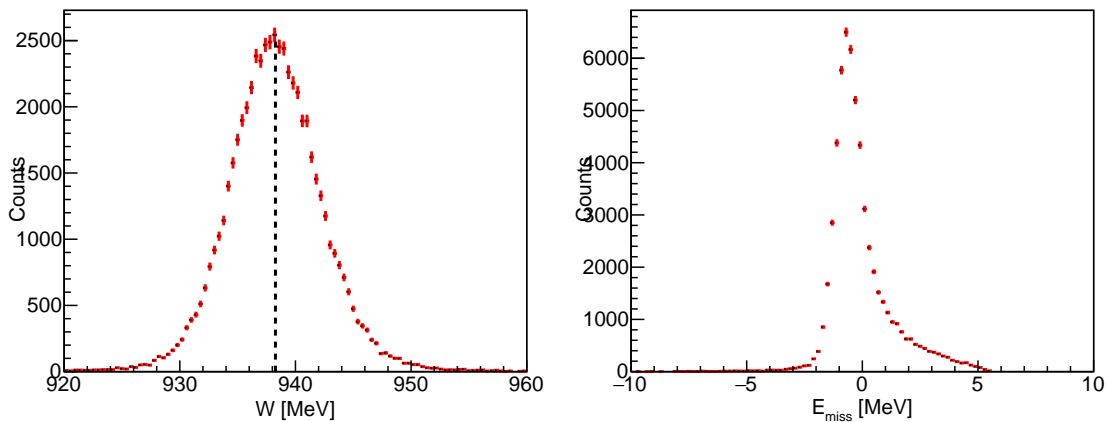


FIG. 17: $H(e, e')$ elastic scattering invariant mass (W) distribution (left) and $H(e, e')p$ missing energy (E_{miss}) distribution (right). The expected W value (shown by the vertical dashed line) is $W = m_p$, where m_p is the proton mass. The standard deviation of the measured W distribution is < 4 MeV.

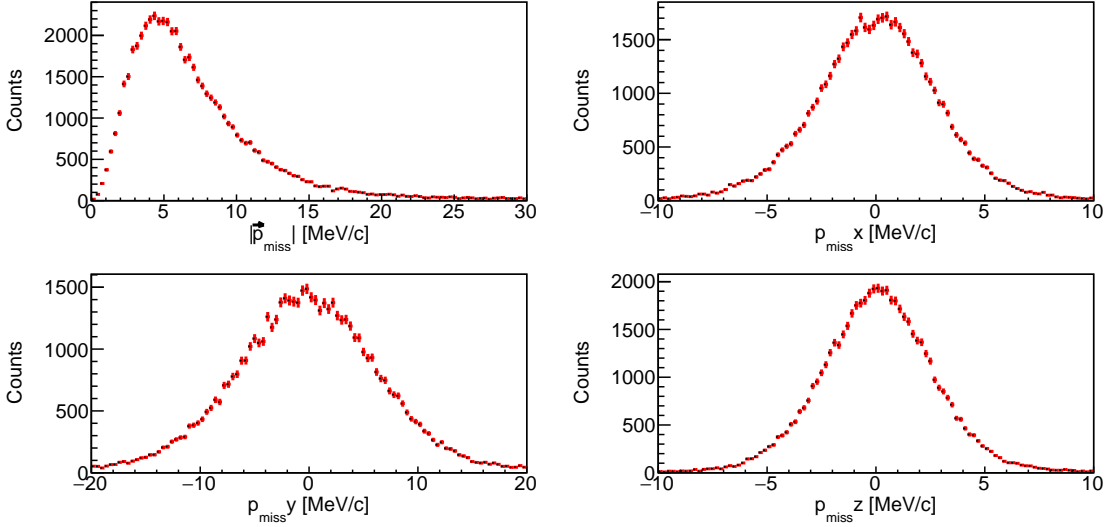


FIG. 18: $H(e, e'p)$ elastic scattering missing momentum magnitude (p_{miss}) and components ($p_{miss i}$, $i = x, y, z$). The square root of the variance of the p_{miss} distribution is < 5.5 MeV/c. The standard deviation of the $p_{miss x}$, $p_{miss y}$, and $p_{miss z}$ distributions are < 3.1 MeV/c, < 6.7 MeV/c, and < 2.3 MeV/c respectively.

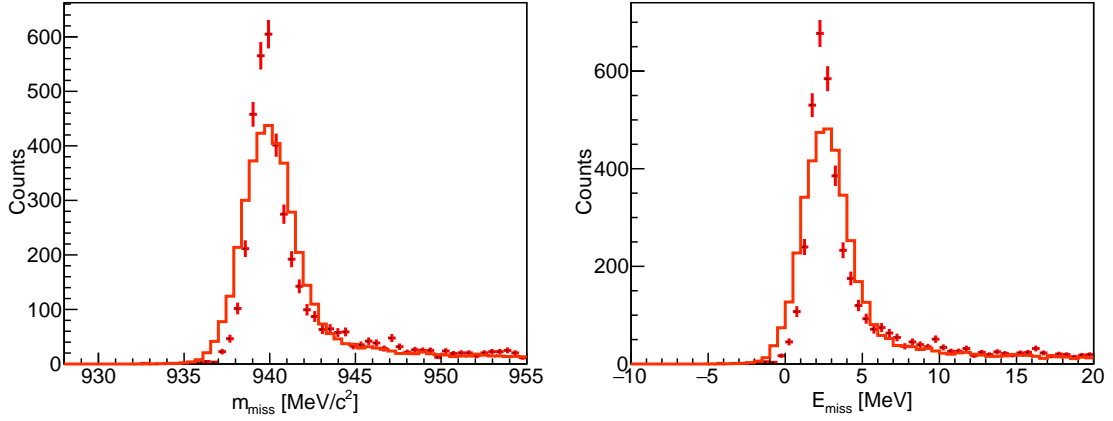


FIG. 19: $D(e, e'p)n$ quasi-elastic scattering missing mass (m_{miss}) distribution (left) and missing energy (E_{miss}) distribution (right). The expected value for the missing mass is $m_{miss} = m_n$, where m_n is the neutron mass. The standard deviation of the measured distribution is < 1.0 MeV. The expected value for the missing energy is $E_{miss} = E_D$, where $E_D = 2.2$ MeV is the deuteron binding energy. The standard deviation of the measured distribution is < 1.0 MeV.

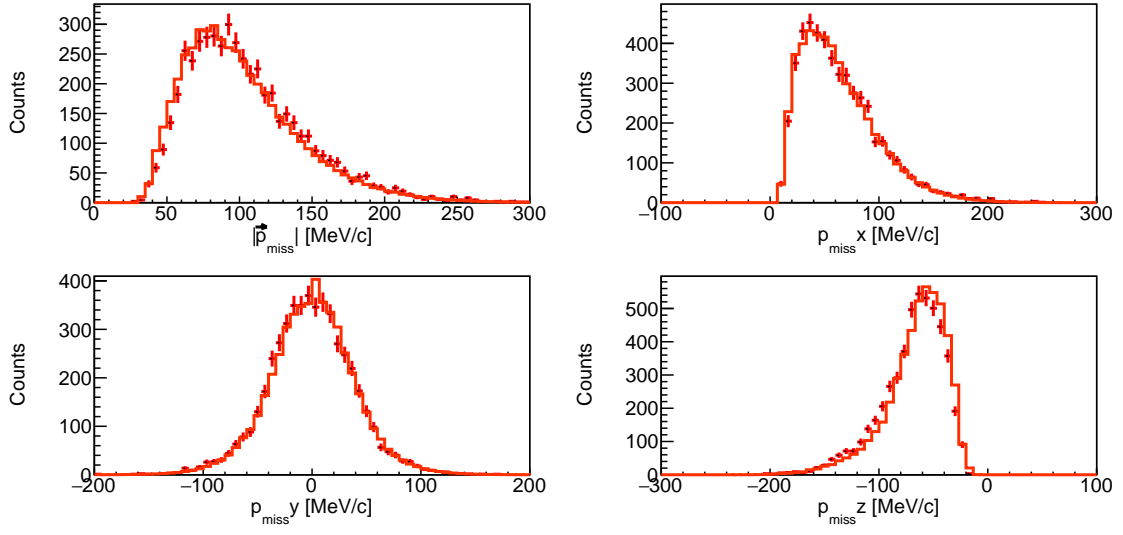


FIG. 20: $D(e, e'p)n$ quasi-elastic scattering missing momentum magnitude (p_{miss}) and components ($p_{miss\ i}$, $i = x, y, z$).